

# **Multi-scale enhanced energy storage performance in Sm(Mg<sub>0.5</sub>Sn<sub>0.5</sub>)O<sub>3</sub>-modified Bi<sub>0.47</sub>Na<sub>0.47</sub>Ba<sub>0.06</sub>TiO<sub>3</sub> ceramics with composite structure**

Yue Pan, Qinpeng Dong, Jiangping Huang, Yu Zhang, Xiuli Chen\*, Xu Li, Lian Deng\*, Huanfu Zhou\*

*Key Laboratory of Nonferrous Materials and New Processing Technology, Ministry of Education, School of Materials*

*Science and Engineering, Guilin University of Technology, Guilin 541004, China.*

---

\* Corresponding authors.

E-mail addresses: cxlnwpu@163.com. (X. Chen), 809188659@qq.com. (L. Deng), zhouhuanfu@163.com. (H. Zhou)

## S1. Experimental procedure

### S1.1 Fabrication of the $x$ SMS ceramics

In this study,  $(1-x)(\text{Na}_{0.47}\text{Bi}_{0.47}\text{Ba}_{0.06}\text{TiO}_3)-x\text{Sm}(\text{Mg}_{0.5}\text{Sn}_{0.5})\text{O}_3$  ( $x = 0.05 \sim 0.25$ ) ceramics were prepared by traditional solid-state reaction method using analytically pure  $\text{Na}_2\text{CO}_3$ ,  $\text{Bi}_2\text{O}_3$ ,  $\text{BaCO}_3$ ,  $\text{TiO}_2$ ,  $\text{Sm}_2\text{O}_3$ ,  $\text{MgO}$  and  $\text{SnO}_2$  as raw materials. The raw materials were stoichiometrically added to a nylon tank and ball-milled with  $\text{ZrO}_2$  balls and ethanol for 12 h. The slurry after ball milling was dried and calcined at  $880\text{ }^\circ\text{C}$  for 4 h, followed by secondary ball milling. The dried powder was added with 5% PVA binder and pressed into 2 mm thick discs. To prevent excessive volatilization of  $\text{Bi}^{3+}$  and  $\text{Na}^+$  during the sintering process, the ceramic embryo was buried in the corresponding calcined powder for burial sintering after debinding at  $650\text{ }^\circ\text{C}$ . The heating rate of the sintering process is  $5\text{ }^\circ\text{C}/\text{min}$  below  $1000\text{ }^\circ\text{C}$ ,  $4\text{ }^\circ\text{C}/\text{min}$  above  $1000\text{ }^\circ\text{C}$ , and holding for 2h. The optimum sintering temperatures of the samples with  $x = 0.05$ ,  $x = 0.10$ ,  $x = 0.15$ ,  $x = 0.20$  and  $x = 0.25$  are  $1220\text{ }^\circ\text{C}$ ,  $1200\text{ }^\circ\text{C}$ ,  $1180\text{ }^\circ\text{C}$ ,  $1160\text{ }^\circ\text{C}$  and  $1155\text{ }^\circ\text{C}$ , respectively.

### S1.2 Characterization

The phase structure of the samples was analyzed by X-ray powder diffractometer (XRD, Model X'Pert PRO; PANalytical, Almelo, Netherlands) under  $\text{Cu } K_\alpha$  radiation, and the data were refined by GSAS software. The microstructure was observed by scanning electron microscopy (FE-SEM, Model S4800, Hitachi, Japan), and the domain morphology and SAED pattern were studied by field emission transmission electron microscopy (FE-TEM, JEM-2100F, JEOL, Tokyo, Japan). The dielectric properties of the ceramics were tested by a precision impedance analyzer (Model 4294A, Hewlett-Packard Co, Palo Alto, CA) in the range from room temperature to  $400\text{ }^\circ\text{C}$ . The ferroelectric properties were evaluated by a ferroelectric material parameter tester (RT66, Radiant Technologies, NM, USA). The thickness of the sample was  $100 \pm 10\text{ }\mu\text{m}$  and the diameter of the silver was 2 mm. The dielectric breakdown strength was tested at RT by a withstand voltage test device (RK2671AM). The Raman spectrum was obtained by a micro-Raman spectrometer (XDR, Thermo Fisher Scientific, USA) with an excitation light source of 532 nm. To check the

domain structure, a piezoresponse force microscope (PFM, MFP-3D, USA) is applied by Pt/Ir-coated conductive tips (Nanosensors, Neuchatel, Switzerland) with an AC tip voltage of 3 V and out-of-plane mode. The underdamped charge-discharge performance was characterized by a dielectric charge-discharge test system (CFD-003, TG Technology, Shanghai, China). The overdamped charge-discharge performance was characterized by a dielectric charge-discharge test system (PK-CPR1701, PolyK Technologies, PA, USA).

## S2. Curie-Weiss law

$$\frac{1}{\varepsilon} - \frac{1}{\varepsilon_m} = \frac{(T - T_m)^\gamma}{C} \quad (\text{S.1})$$

where  $\varepsilon_m$  is the maximum dielectric constant and  $\gamma$  is the dispersion coefficient. The dispersion coefficient  $\gamma$  characterises the degree of relaxation of the ceramic material, when  $\gamma = 1$  indicates an ideal ferroelectric phase transition with a sharp peak, while  $\gamma = 2$  exhibits a strongly dispersive phase transition.

## S3. $\Delta T_{\text{relaxor}}$

$$\Delta T_{\text{relaxor}} = T_s(10\text{kHz}) - T_s(1\text{MHz}) \quad (\text{S.2})$$

where  $T_s(10\text{ kHz})$  and  $T_s(1\text{ MHz})$  are the values of  $T_s$  at frequencies of 10 kHz and 1 MHz, respectively, as identified on the dielectric temperature spectrum.

## S4. Curie-Weiss model and Vogel-Fulcher theory

According to the Curie-Weiss model and Vogel-Fulcher theory, the calculation formula is as follows <sup>1,2</sup>:

$$\varepsilon_r = \frac{C}{T - T_{CW}} \quad (\text{S.3})$$

$$f = f_0 \frac{-E_a}{e^{k_B(T_s - T_f)}} \quad (\text{S.4})$$

where  $C$  and  $T_{CW}$  are the Curie constant and the Curie-Weiss temperature, respectively;  $f$  is the test frequency;  $T_s$  is extracted from the  $\varepsilon_r(T)$  curve;  $f_0$  is the characteristic frequency (dynamic transition frequency/ion attempt jump barrier frequency in the double-well model);  $E_a$  is the activation energy.

## S5. Pulse charge/discharge key performance parameters calculation formula

The main performance parameters of pulse charging and discharging: discharge density ( $W_{\text{dis}}$ ), power

density ( $P_D$ ) and current density ( $C_D$ ) are calculated as follows <sup>3</sup>:

$$W_{\text{dis}} = R \int i^2(t) dt / V \quad (\text{S.5})$$

$$C_D = I_{\text{max}} / S \quad (\text{S.6})$$

$$P_D = EI_{\text{max}} / 2S \quad (\text{S.7})$$

where  $R$  is the test resistance,  $V$  is the sample volume,  $S$  is the backsilver area, and  $E$  is the electric field strength.

## **S6. Ergodic relaxation phase and non-ergodic relaxation phase**

The two characteristic temperatures related to ergodic relaxation phase (ER) and non-ergodic relaxation phase (NER) are the burning temperature ( $T_B$ ) and the freezing temperature ( $T_f$ ), respectively. Above the characteristic temperature  $T_B$ , the RFE are in paraelectric phase. When the temperature begins to decrease from above  $T_B$ , PNRs begin to appear in the cubic matrix. At higher temperatures, the density of PNRs is low, and they are dispersed in the paraelectric phase matrix of the cubic structure in an island shape. The polarization vector of PNRs is a function of time and position, which is called ER <sup>4</sup>. As the temperature further decreases, the density of PNRs becomes larger and larger. At the same time, small-sized PNRs can get rid of thermal activation and merge to form larger-sized PNRs (nanodomains or microdomains). When the temperature is lower than the  $T_f$ , the polarization vector of PNRs is no longer dependent on time, but only related to position, which is called NER <sup>5</sup>. The main difference between the ferroelectric states of ER and NER is that NER irreversibly transforms into a long-range ferroelectric phase under an applied electric field, whereas in ER the field-induced relaxor-ferroelectric transition is reversible.

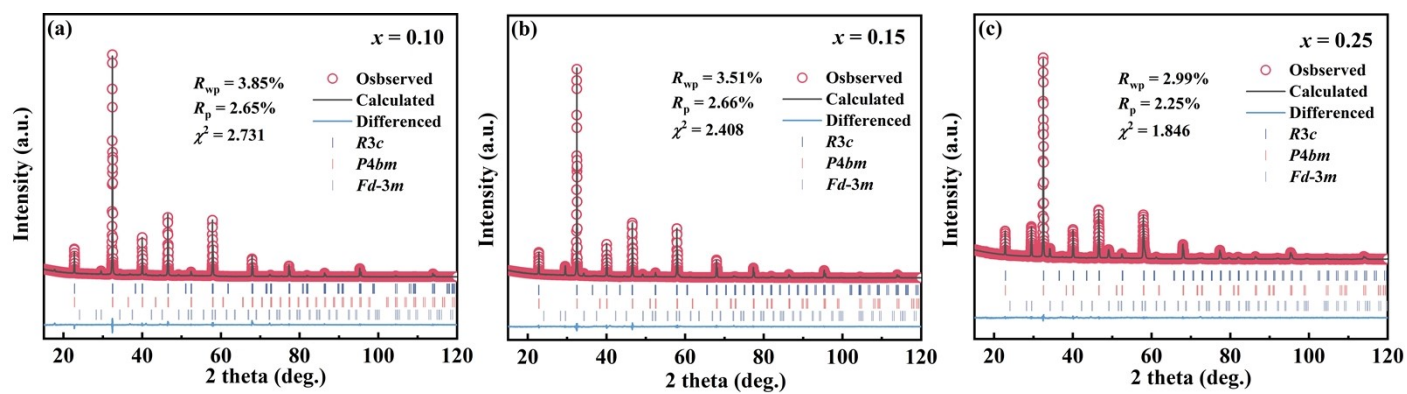


**Fig. S1.** Rietveld refinement plots of  $100x$ SMS ceramics: (a)  $x = 0.10$ , (b)  $x = 0.15$ , (c)  $x = 0.25$ .

**Table. S1.** Room-temperature refined structural parameters of the 100xSMS ceramic powders

<i>x</i>	Space group	Lattice parameters	V (Å <sup>3</sup> )	<i>R</i> <sub>wp</sub> (%)	<i>R</i> <sub>p</sub> (%)	χ <sup>2</sup>
0.05	<i>R3c</i> (72.32%)	a = b = 5.5044(1), c = 13.5678(2), α = β = 90°, γ = 120°	356.010	3.83	2.80	2.489
	<i>P4bm</i> (27.68%)	a = b = 5.5200(0), c = 3.9040(5), α = β = γ = 90°	118.958			
0.10	<i>R3c</i> (55.05%)	a = b = 5.5133(2), c = 13.5208(0), α = β = 90°, γ = 120°	355.926	3.85	2.65	2.731
	<i>P4bm</i> (43.98%)	a = b = 5.5128(4), c = 3.8999(8), α = β = γ = 90°	118.526			
	<i>Fd-3m</i> (0.97%)	a = b = c = 10.4567(4), α = β = γ = 90°	1143.378			
0.15	<i>R3c</i> (51.90%)	a = b = 5.5134(8), c = 13.5121(9), α = β = 90°, γ = 120°	355.720	3.51	2.66	2.408
	<i>P4bm</i> (46.69%)	a = b = 5.5183(0), c = 3.9062(3), α = β = γ = 90°	118.952			
	<i>Fd-3m</i> (1.41%)	a = b = c = 10.4693(6), α = β = γ = 90°	1147.521			
0.20	<i>R3c</i> (43.72%)	a = b = 5.5131(1), c = 13.5111(8), α = β = 90°, γ = 120°	355.646	3.11	2.31	1.834
	<i>P4bm</i> (52.85%)	a = b = 5.5117(6), c = 3.8959(5), α = β = γ = 90°	118.357			
	<i>Fd-3m</i> (3.43%)	a = b = c = 10.4894(2), α = β = γ = 90°	1154.131			
0.25	<i>R3c</i> (34.70%)	a = b = 5.5125(1), c = 13.5089(7), α = β = 90°, γ = 120°	355.511	2.99	2.25	1.846
	<i>P4bm</i> (56.32%)	a = b = 5.5057(9), c = 3.8938(3), α = β = γ = 90°	118.037			
	<i>Fd-3m</i> (8.98%)	a = b = c = 10.4947(2), α = β = γ = 90°	1155.880			

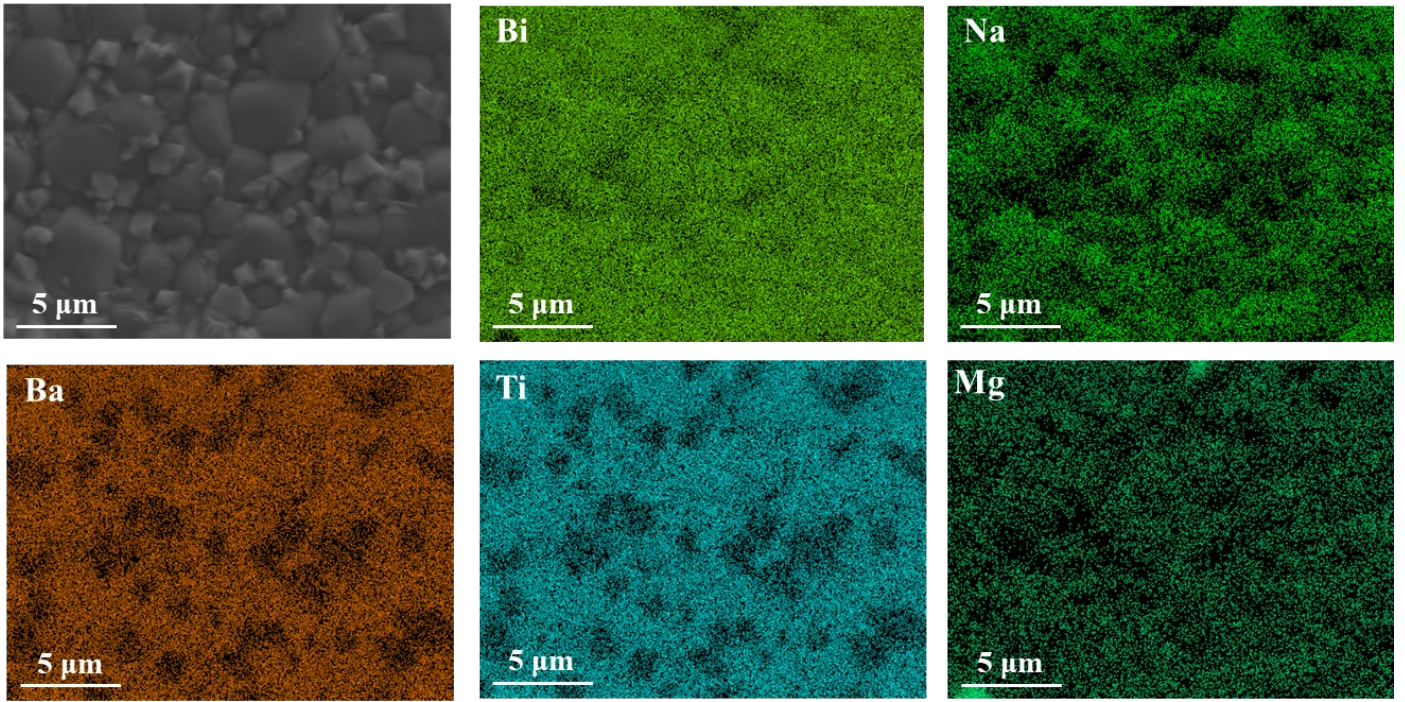


**Fig. S2.** EDS mapping images of 20SMS ceramics.

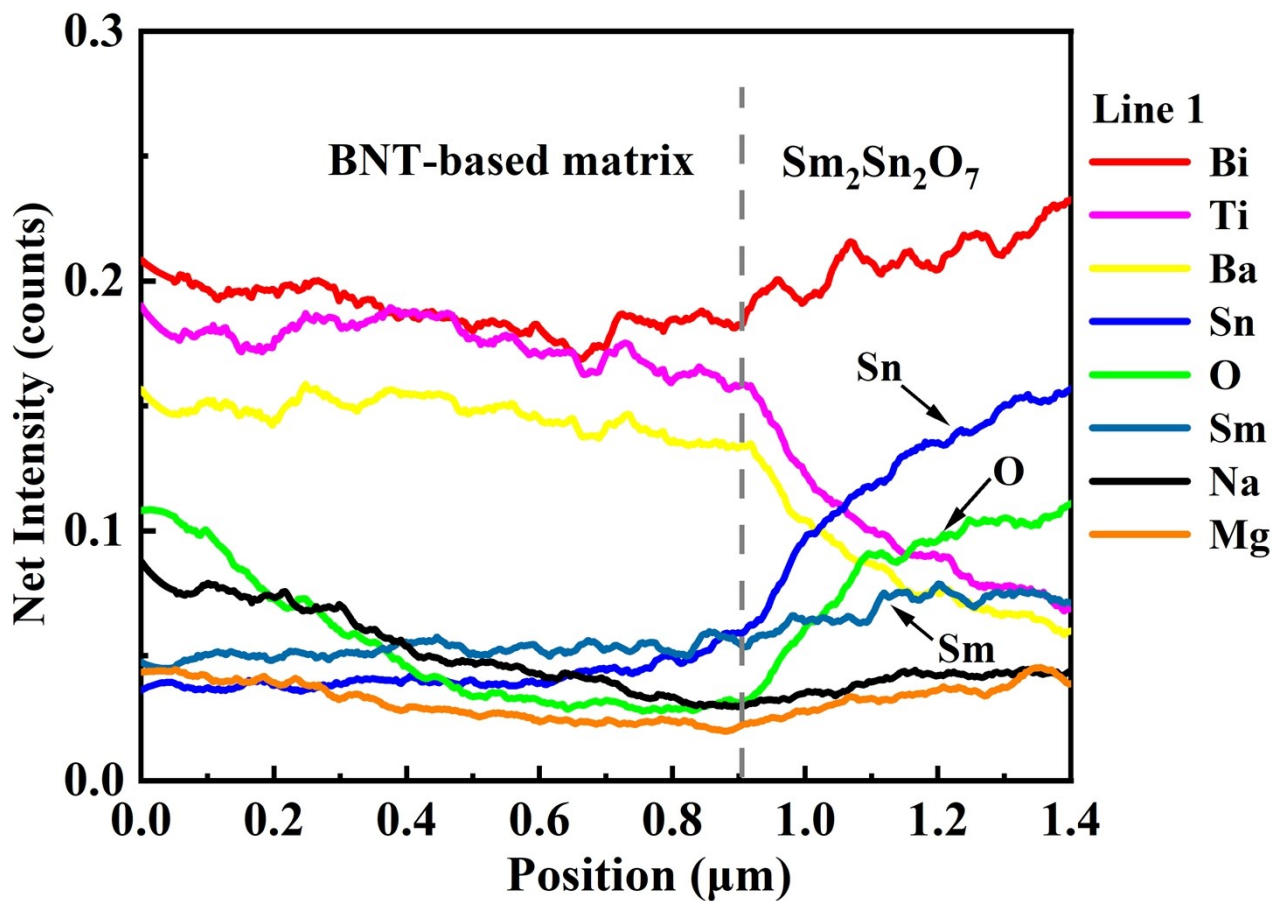
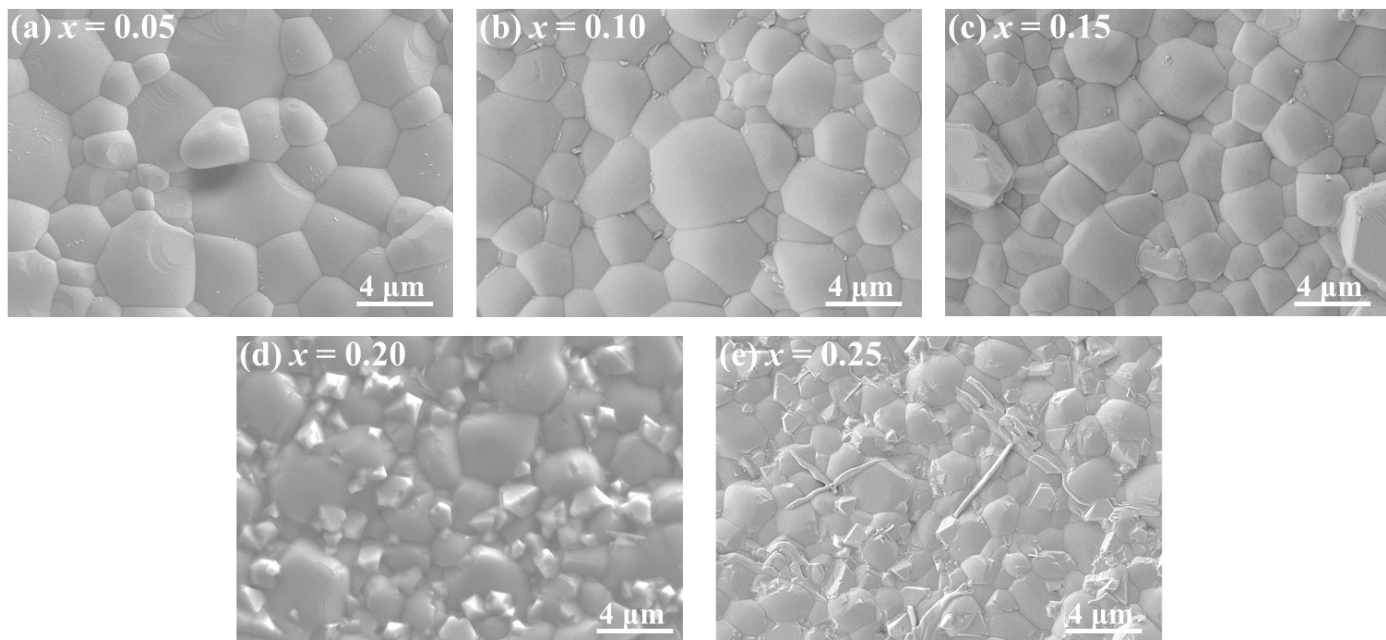


Fig. S3. EDS line scan analysis results across the BNT-based matrix/ $\text{Sm}_2\text{Sn}_2\text{O}_7$  interface (line 1).

**Table. S2.** EDS analysis results of 20SMS ceramics at various positions

<b>Element</b>	<b>Point 1</b>	<b>Point 2</b>
<b>Bi</b>	<b>9.85</b>	<b>8.04</b>
<b>Na</b>	<b>7.97</b>	<b>/</b>
<b>Ba</b>	<b>2.24</b>	<b>/</b>
<b>Ti</b>	<b>20.70</b>	<b>6.27</b>
<b>Sm</b>	<b>4.39</b>	<b>8.04</b>
<b>Mg</b>	<b>2.61</b>	<b>1.40</b>
<b>Sn</b>	<b>1.85</b>	<b>9.47</b>
<b>O</b>	<b>50.39</b>	<b>69.28</b>



**Fig. S4.** The SEM images of 100xSMS ( $x = 0.05, 0.10, 0.15, 0.20, 0.25$ ) ceramics.

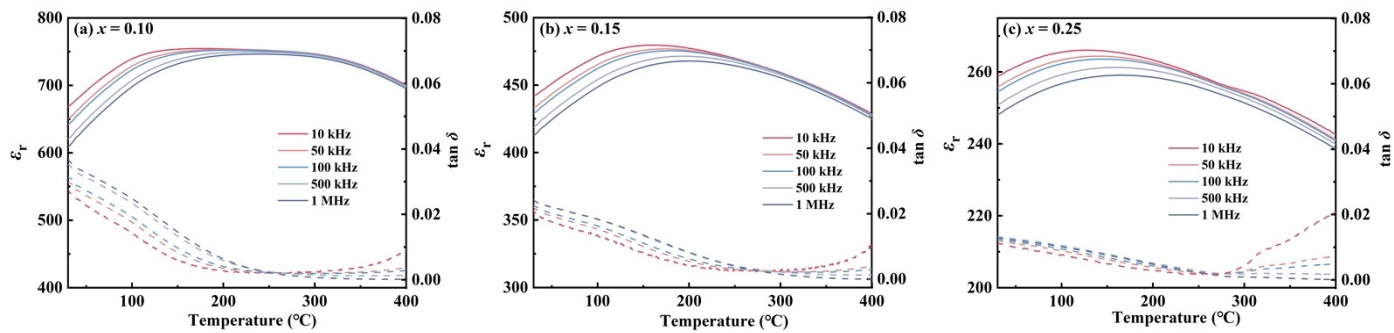


**Fig. S5.** Temperature dependences of the  $\epsilon_r$  and  $\tan \delta$  of 10SMS, 15SMS and 20SMS ceramics at various frequencies.

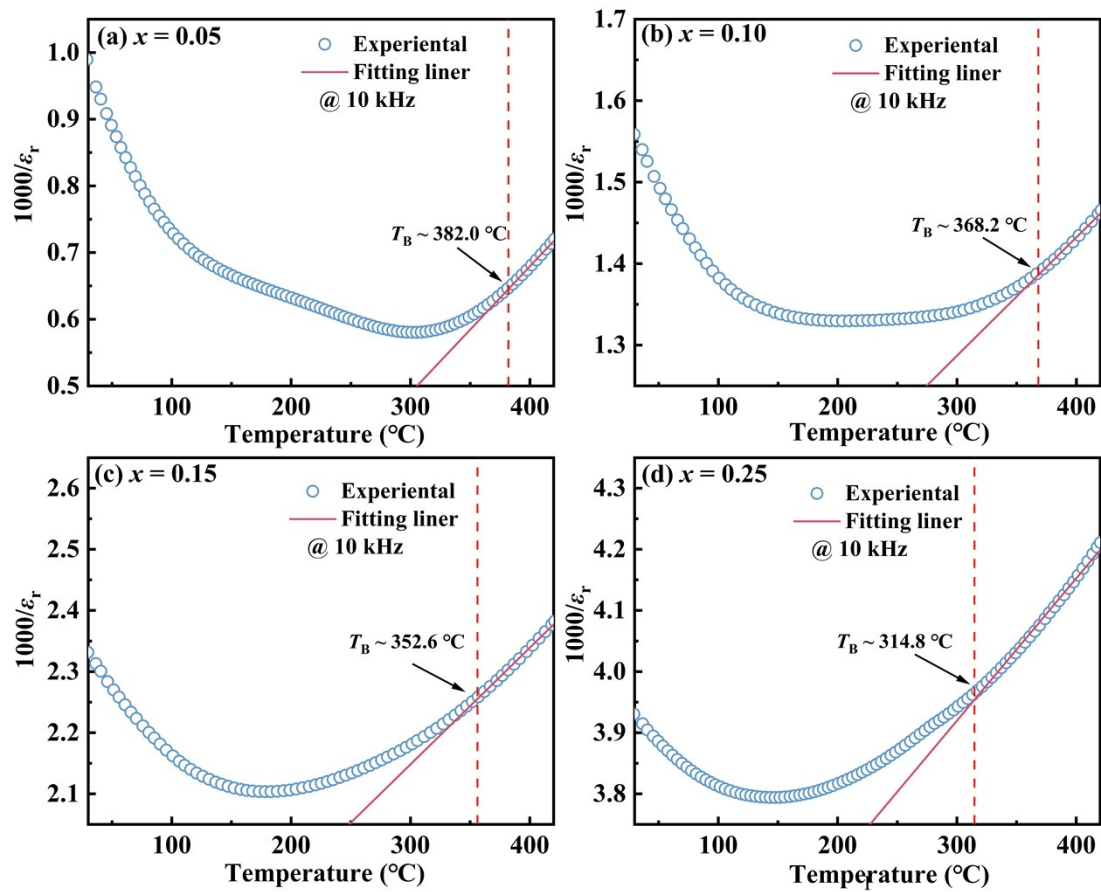


**Fig. S6.** Temperature dependence of  $1/\epsilon_r$  in 100xSMS ceramics: (a)  $x = 0.05$ , (b)  $x = 0.10$ , (c)  $x = 0.15$  and (d)  $x = 0.25$ .

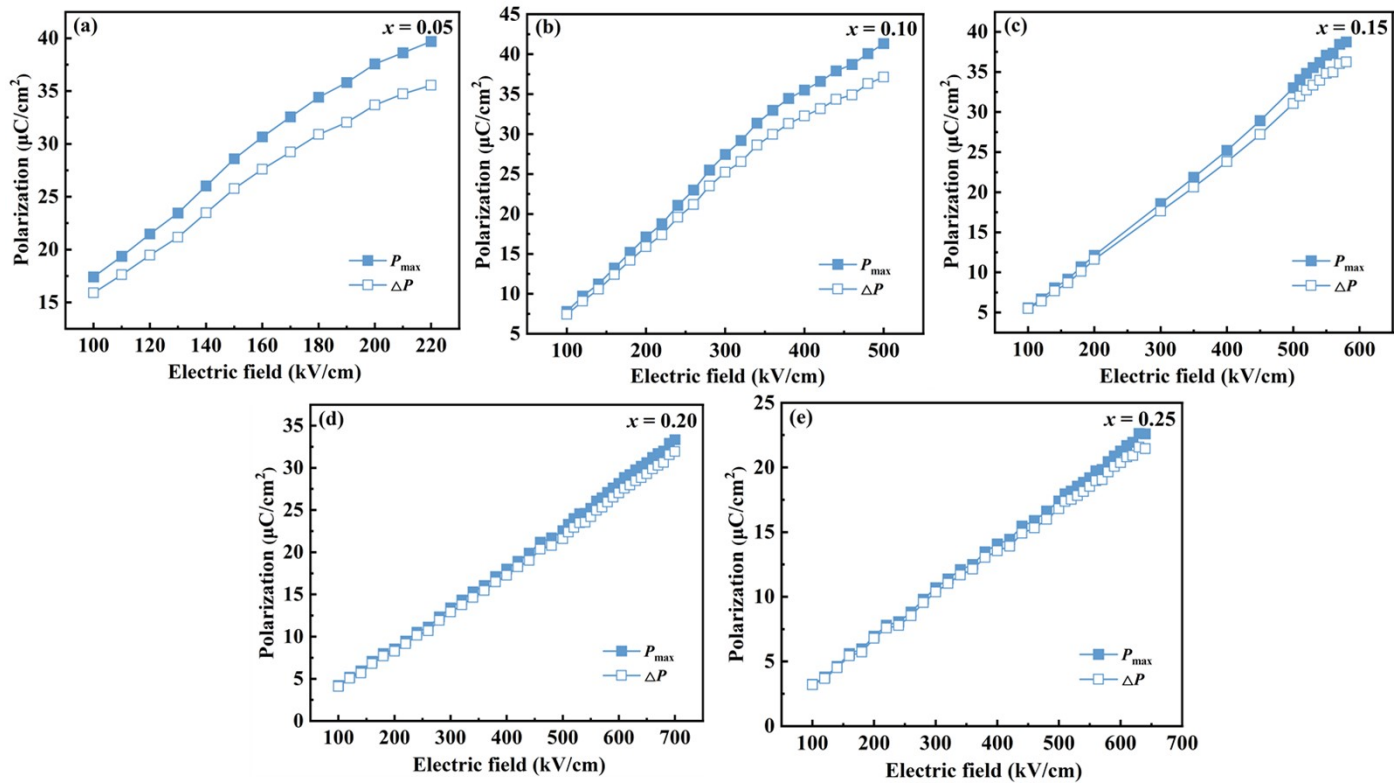


**Fig. S7.** The changes of  $P_{\text{max}}$ ,  $\Delta P$  with electric fields for 100xSMS ceramics: (a)  $x = 0.05$ , (b)  $x = 0.10$ , (c)  $x = 0.15$ , (d)  $x = 0.20$  and (e)  $x = 0.25$ .

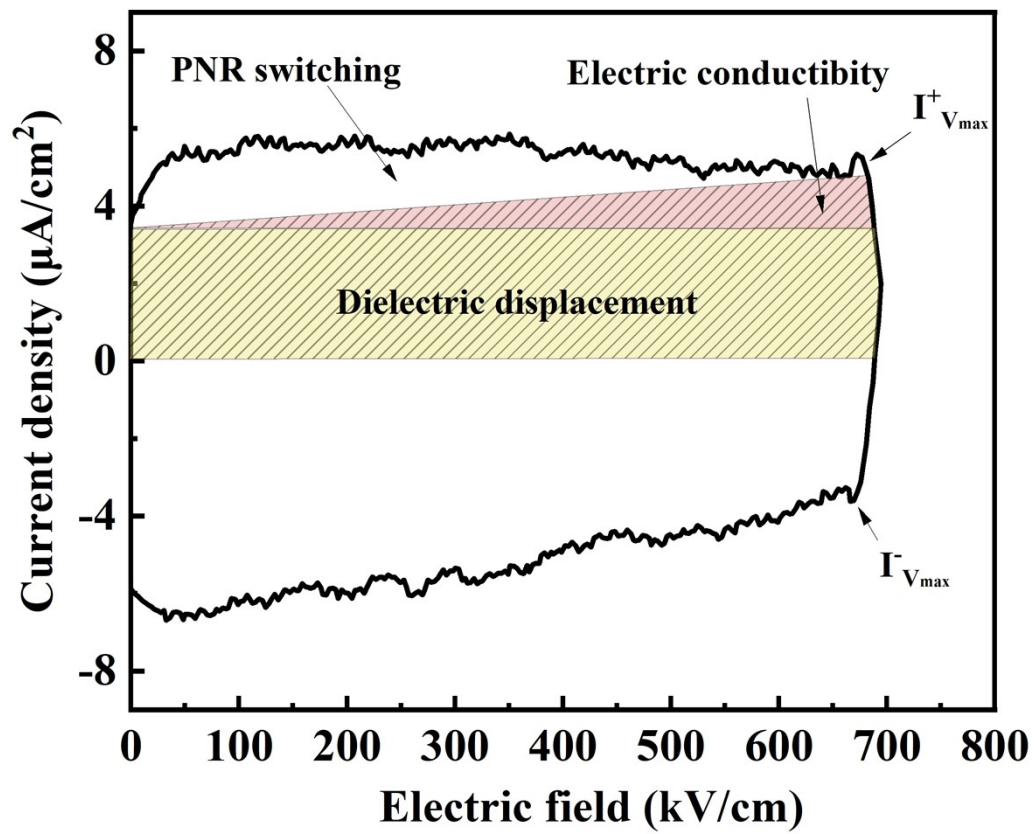
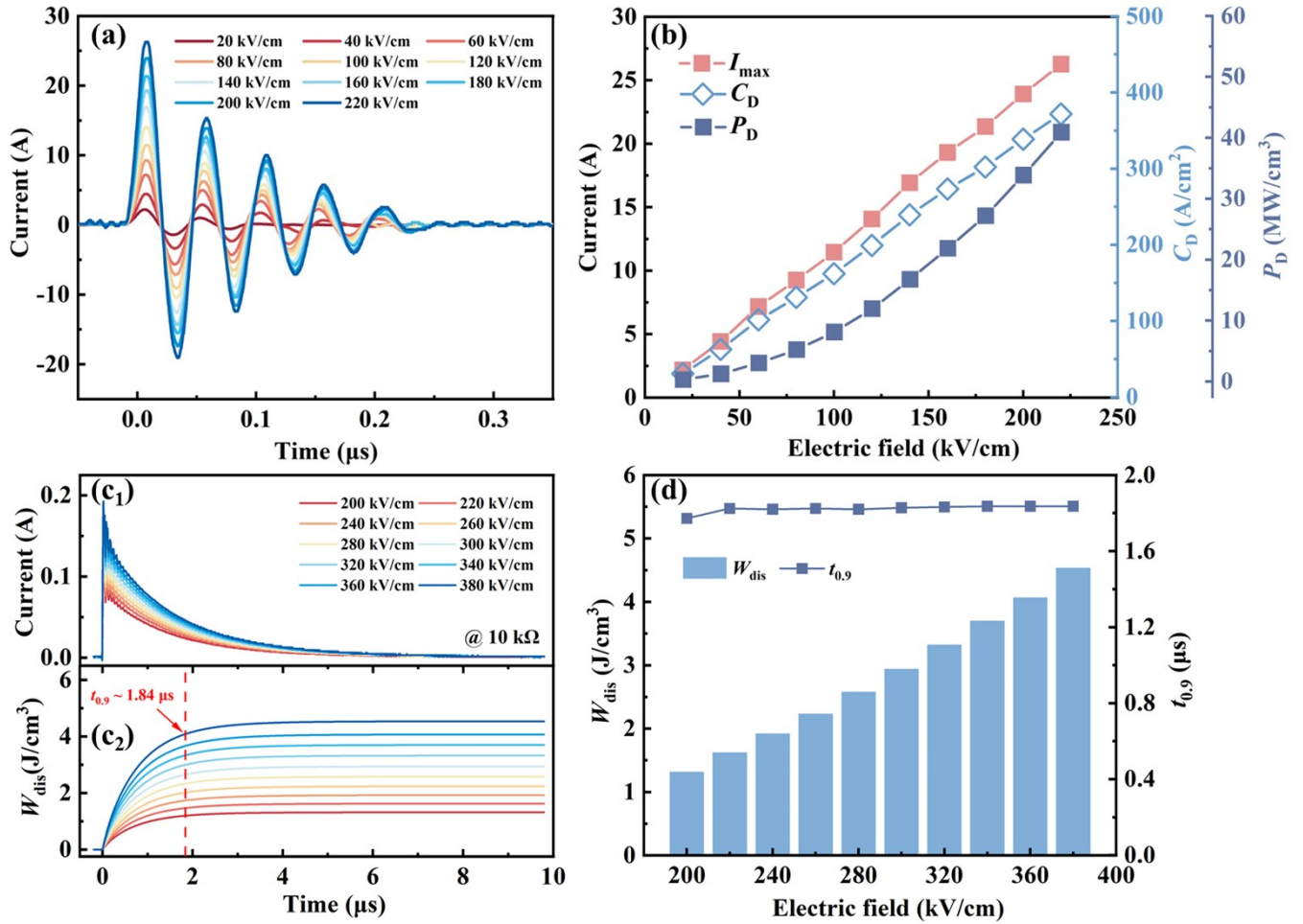


Fig. S8. The  $I$ - $E$  loop of the 20SMS ceramic.



**Fig. S9.** (a, b) Test results of under-damped discharge of 20SMS ceramics at different electric fields. (c<sub>1</sub>, c<sub>2</sub>) Test results of 20SMS ceramics overdamped discharge at different electric fields (load: 10 kΩ). (d) The variation of  $W_{\text{dis}}$  and  $t_{0.9}$  with the electric field.

To better measure the actual discharge performance of dielectric ceramics, Fig. S9(a) shows the underdamped discharge curve of 20SMS ceramics. From the diagram, it can be seen that the maximum current ( $I_{\max}$ ) increases with the increase of the electric field, and the waveform of the underdamped curve does not change significantly, indicating that the 20SMS ceramic has a stable discharge cycle. The variation of key performance parameters [ $I_{\max}$ , current density ( $C_D$ ) and power density ( $P_D$ )] with electric field is shown in Fig. S9(b). It can be seen from the figure that  $I_{\max}$  increases from 2.18 A to 26.27 A. At 220 kV/cm,  $C_D$  and  $P_D$  were 371.79 A/cm<sup>2</sup> and 40.90 MW/cm<sup>3</sup>, respectively. To further measure the actual discharge capacity of 20SMS ceramics, Fig. S9(c<sub>1</sub>, c<sub>2</sub>) shows the overdamped discharge curves of 20SMS ceramics and the relationship between discharge energy density ( $W_{\text{dis}}$ ) and electric field. It is easy to see from the

figure that the current values of 20SMS ceramics can peak quickly under different electric fields and decay in microseconds, which is consistent with the overdamped discharge model. According to Fig. S9(c<sub>1</sub>, c<sub>2</sub>), the relationship between the main performance parameters [ $I_{\max}$ ,  $W_{\text{dis}}$  and discharge time ( $t_{0.9}$ )] and the electric field is obtained. With the increase of the electric field,  $I_{\max}$  rises from 0.10 A at 200 kV/cm to 0.19 A at 380 kV/cm, and  $W_{\text{dis}}$  reaches its maximum value of 4.54 J/cm<sup>3</sup> at 380 kV/cm. Compared to the  $W_{\text{rec}}$  value (2.94 J/cm<sup>3</sup>) estimated from the  $P$ - $E$  hysteresis loop at the same field strength,  $W_{\text{dis}}$  is significantly higher than  $W_{\text{rec}}$ , which can be attributed to the current differences between the two testing methods. It is worth noting that the obvious dielectric (capacitive) nonlinearity induced by the electric field in ferroelectric materials leads to the attenuation of  $t_{0.9}$ . However, the decrease of  $t_{0.9}$  with increasing electric field in 20SMS ceramics is not obvious and is maintained at about 1.84  $\mu$ s, indicating that the capacitance of 20SMS ceramics is insensitive to the external electric field, which further confirms the existence of weakened nonlinear polarization response behavior in this system.

## References

1. D. Viehland, S. J. Jang, L. E. Cross and M. Wuttig, *J. Appl. Phys.*, 1990, **68**, 2916-2921.
2. C. Ang, Z. Yu and Z. Jing, *Phys. Rev. B*, 2000, **61**, 957-961.
3. J. M. Ye, G. S. Wang, M. X. Zhou, N. T. Liu, X. F. Chen, S. Li, F. Cao and X. L. Dong, *J. Mater. Chem. C*, 2019, **7**, 5639-5645.
4. C. W. Ahn, C.-H. Hong, B.-Y. Choi, H.-P. Kim, H.-S. Han, Y. Hwang, W. Jo, K. Wang, J.-F. Li, J.-S. Lee and I. W. Kim, *J. Korean Phys. Soc.*, 2016, **68**, 1481-1494.
5. A. Peláiz-Barranco, F. Calderón-Piñar, O. García-Zaldívar and Y. González-Abreu, *Advances in Ferroelectrics*, 2012, **13**, 85-107.